A Study of Embryo Production and Hail Growth Using Dual-Doppler and Multiparameter Radars

JOHN W. CONWAY

Aeroment, Inc., Kwajalein, Marshall Islands

DUŠAN S. ZRNIĆ

National Severe Storms Laboratory, Norman, Oklahoma

(Manuscript received 29 October 1992, in final form 1 March 1993)

ABSTRACT

The origin and importance to embryo and hail production of a region of drops advected above the freezing level in the updraft of a severe Colorado hailstorm is examined using radar polarization measurements in conjunction with dual-Doppler and trajectory analysis. These drops, which give a distinct radar signature termed the "differential reflectivity column," originate from 1) melted hydrometeors that fall from the back-sheared anvil, through the embryo curtain, and are recirculated into the storm updraft, and 2) in situ drop growth within the updraft. Some of the drops refreeze and likely produce frozen-drop hailstone embryos.

Numerous hailstone trajectories are found to cross either through, or over, the drop column where the hailstones undergo a significant growth phase. Two separate hailstone fallout regions are identified. Some hailstones in the northern fallout region show anticyclonic trajectories and in situ updraft and column growth. Others grow while crossing the top of the vault. Hailstones in the southern region exhibit growth while passing cyclonically through the column or over the vault.

A new method to determine hydrometeor fall speeds from radar polarization measurements for use with dual-Doppler analysis is introduced.

1. Introduction

Recent studies of hailstorms using Doppler radar and trajectory analysis have provided a wealth of information for inclusion in models and have improved conceptual understanding of some complexities of hailstorm dynamics and microphysics. A significant enhancement in the observational techniques occurred with the advent of multiparameter radars. Notable among these is the radar polarization technique that allows discrimination of some hydrometeor types, including hail. Yet to date, because of limitations in data collection and analysis, a large amount of speculation still exists as to the origin of hailstone embryos and growth trajectories. This study uses radar-derived kinematics, trajectory analysis, and polarization variables concurrently to substantiate existing theories of hailstone origin and growth in a severe Colorado hailstorm.

Browning and Foote (1976) formulated the first complete conceptual model of hail formation in supercell storms based on the equivalent reflectivity factor Z_e structure of a northeast Colorado hailstorm. They concluded that three main trajectories exist for the possible origins of hailstone embryos and their subsequent growth. These are 1) trajectories in which embryos enter the main updraft and exit in the forward (downwind) anvil and thus do not contribute to the main hail shaft; 2) trajectories that enter the less intense western periphery of the main updraft where embryos grow in their ascent—some fall cyclonically from the upwind midlevel stagnation area and enter the embryo curtain (reflectivity overhang) where they encounter further but slower growth; 3) trajectories of embryos that fall through the bottom of the embryo curtain (due to their larger size), reenter the foot of the main updraft, and grow more rapidly due to the larger liquid water content (LWC). Furthermore, Browning and Foote (1976) proposed the largest hailstones came from embryos that fell from the embryo curtain and reentered the main updraft at an altitude where a balance could be achieved between embryo (or hailstone) growth, fall speed, and updraft velocity.

Recent studies have used microphysical growth equations and/or Doppler-derived wind fields to reconstruct trajectories from which hail embryo sources and growth were deduced (e.g., Heymsfield et al. 1980; Heymsfield 1982; Nelson 1983; Ziegler et al. 1983). In this literature several possible embryo sources are discussed. The relative importance of these sources is

Corresponding author address: Dr. Dušan S. Zrnić, NOAA/NSSL, Doppler Radar and Remote Sensing Research Group, 1313 Halley Circle, Norman, OK 73069.

reviewed and summarized by Foote (1985). Since then other studies have emerged that have extended the previous findings (e.g., Nelson and Knight 1987; Miller et al. 1990; Bluestein and Woodall 1990).

After the initial embryo growth stage, hailstones are thought to follow three main trajectories. The first is the recycling trajectory shown as A in Fig. 1 whose fallout is generally confined to the middle of the hail cascade, just north and west of the main updraft. A second trajectory arises from hailstones grown within the southwestern edge of the updraft in the anticyclonic streamflow downwind of the stagnation point (Miller et al. 1990; Bluestein and Woodall 1990) (Fig. 1 trajectory B). This path leads to an abundant but smaller size hail fall in the northern section of the main core. The final main trajectory passes through the center of the updraft at midlevels (across the vault) where higher LWC of 3–4 g m^{-3} and in cloud temperatures (−15° to −20°C) predominate, that is, a "prime growth zone" (Ziegler et al. 1983) (Fig. 1, trajectory C). This trajectory, likely responsible for the largest hail sizes, stays near the center of rotation where horizontal displacements are minimized and thus residence time in the updraft is increased (Miller et al. 1990). Most favorable conditions for growth again occur when the terminal fall speeds are matched to the updraft velocities. The fallout region of this lower concentration of larger hail is to the rear of the main updraft. Our study finds the majority of hailstone trajectories to follow one of these three paths. We also find that a number of hailstone paths originate in the ambient storm inflow. These paths suggest that hailstones grow in a single up–down traverse of the updraft.

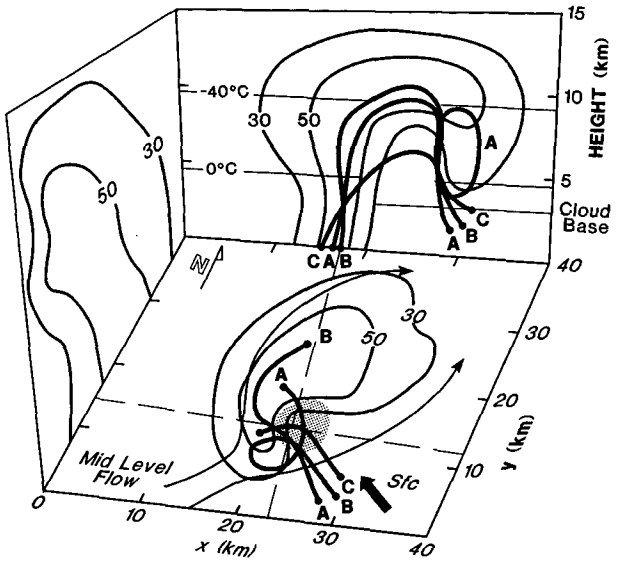

FIG. 1. Conceptual model of hailstone trajectories within a supercell storm. The equivalent reflectivity factor Z_e contours are in dBZ. Arrows represent storm relative midlevel flow. The bold arrow represents surface flow. The stippled region is the main updraft core. Path A represents common embryo recycling, B corresponds to growth in anticyclonic streamflow, and C represents the trajectory leading to largest hail growth.

Until the advent of radar polarization measurements, hydrometeor type, shape, and orientation throughout the volume of a convective storm could not be quickly measured nor a direct relationship to storm processes established (Seliga and Bringi 1976). Recently, several investigators have discovered distinct relations between radar polarization signals and cloud microphysics. From these it was possible to identify hail locations at the surface (e.g., Herzegh and Jameson 1992; Meischner et al. 1991; Aydin et al. 1990, 1986; Tuttle et al. 1989; Bringi et al. 1986a,b; Illingworth et al. 1986), hail aloft (Meischner et al. 1991; Aydin et al. 1990; Herzegh and Jameson 1992; Tuttle et al. 1989), and mixed-phase regions above the freezing level (Herzegh and Jameson 1992; Liu and Herzegh 1986).

In some convective settings, clear evidence of "differential reflectivity (Z_{DR}) columns" (Meischner et al. 1991; Tuttle et al. 1989; Illingworth et al. 1987; Caylor and Illingworth 1987) was obtained. These positive Z_{DR} signatures, with values as high as 6 dB, are thought to be drops that are formed through the warm-rain coalescence process or melting of ice hydrometeors, and are advected above the freezing level within updrafts. In hailstorms containing a single main updraft, the origin of the Z_{DR} column and its importance to the hail production process need further clarification.

The purpose of this study is to examine, through polarization signatures, Doppler wind-field retrieval, and particle trajectory analysis, a Z_{DR} column that extended to over 2.5 km above the environmental freezing level and coincided with the updraft of a severe Colorado hailstorm. By examining trajectories that pass through the column or end at the location of hail on the surface, we establish a possible relationship between the Z_{DR} column and hail formation processes in the storm. The following section provides a synopsis of the event followed by a description of the data analysis techniques, including an overview of dual-polarization signatures. Dual-Doppler and trajectory methodologies are then described. The remaining sections present and summarize the results from this case study.

2. Storm overview

On 13 June 1984, a series of severe hailstorms, exhibiting supercell and multicell characteristics, devastated the northern and eastern suburbs of Denver, Colorado, with hail up to 9 cm in diameter. Some areas received large hail for periods of 40 min. One fatality, 22 injuries, and over $350 million damage made this one of the worst hailstorm events in United States history.

Available observations include mesonet data obtained by the Program for Regional Observing and

Forecasting Services (PROFS) and hourly wind data from the National Oceanic and Atmospheric Administration Wave Propagation Laboratory (NOAA WPL) profiler located at the Denver National Weather Service Forecast Office (DEN NWSFO). In support of the May Polarization Experiment (MAYPOLE 84), the National Center For Atmospheric Research (NCAR) CP-2 radar (wavelength 10 cm) collected reflectivity, velocity, and polarization data, while the CP-4 radar (wavelength 5 cm) collected reflectivity and velocity data. Surface hail was collected for a brief period. The CP-2 was also equipped with orthogonally mounted, matched beamwidth, 3.2-cm (X band) transmitting and receiving antennas; this allowed recording of other variables in addition to Z_{DR} and comparisons of reflectivities at the two wavelengths. The CP-2 was inoperable between 1430 and 1550 LST (LST is 6 h behind the universal coordinated time) due to a lightning strike, a period corresponding to the occurrence of largest hail (9 cm), as reported by the National Weather Service (NWS) spotters. The observation platforms and regional location are depicted in Fig. 2, whereas radar characteristics are in Table 1. Blanchard and Howard (1986) provide a detailed overview of this event, including profiler observations and storm photographs.

The synoptic and mesoscale settings were typical of severe weather outbreaks in postfrontal upslope flow found in the Colorado eastern plains (e.g., Maddox et al. 1981; Doswell 1980). Surface high pressure in southern South Dakota advected moisture with 13°–16°C dewpoints on southeasterly flow against the Front Range. Aloft, increasing southwesterly flow, as shown by profiler data, caused differential advection of air containing steep midlevel lapse rates (8.5°C km^{-1}) over the deep surface moisture. Storms formed over the mountains and moved eastward over the Denver area.

TABLE 1. Doppler radar characteristics.

	S band CP-2	X band CP-2	C band CP-4
Wavelength	10.67 cm	3.20 cm	5.49 cm
Average transmittal power	61 dBm	45.6 dBm	55.3 dBm
Pulse length	150 m	150 m	150 m
Gate spacing	200 m	200 m	160 m
Beamwidth	0.96°	0.95°	1.1°
Nyquist velocity	±12 m s^{-1}	NA	±18 m s^{-1}

Figure 3 shows an estimate of the DEN sounding for 1400 LST. This was obtained by examination of the 1200 UTC DEN sounding and considerations of upstream differential temperature advection from other 1200 UTC soundings. Using the 1400 LST DEN surface observations with the estimated 1400 LST sounding we determined that the environment was characterized by moderate instability with convective available potential energy (CAPE) of 2350 J kg^{-1} for parcels ascending from the level of free convection (LFC) at 680 mb. After reaching this level, parcels ascend along the pseudoadiabat corresponding to an equivalent po-

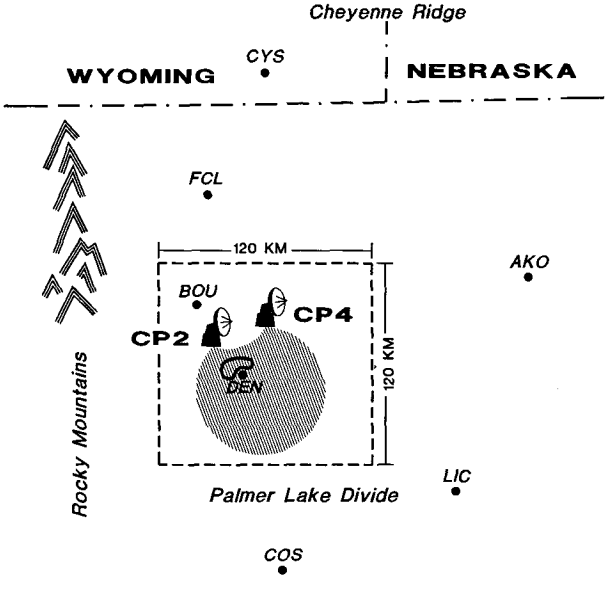

FIG. 2. Analysis region with main terrain features and NWS identifiers. The shaded area represents the dual-Doppler lobe used in analysis. The outlined area within the shading is the storm location at the analysis time (1750 LST).

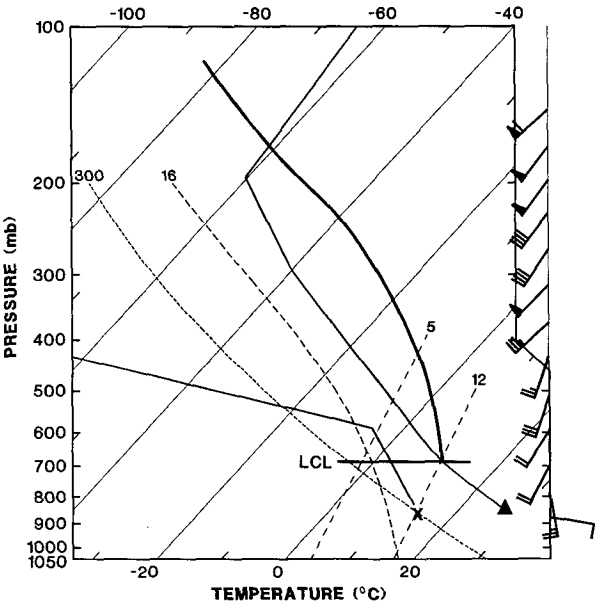

FIG. 3. Sounding considered valid for 1400 LST based on upstream differential temperature advection from DEN. Mixing ratio lines (g kg^{-1}) slant upward left to right. Dry adiabat (dashed) slants right to left. Solid lines with "X" and "Δ" at base are environmental dewpoint and temperature profiles. The bold solid line represents parcel ascent from LFC. Winds plotted are from 1400 LST profiler observations. Half-barb is 2.5 m s^{-1}, full barb is 5 m s^{-1}, and flag is 25 m s^{-1}.

tential temperature θ_e = 349 K giving a lifted index (LI) of −8°C at 500 mb. The environmental freezing level is approximately 2.7 km above ground level (AGL), while the in-cloud freezing level is about 4 km AGL. The 500-m-to-6-km shear, as derived from the 1400 LST profiler observations, is a moderate value of 5.8×10^{-3} s^{-1}. The buoyancy and shear values produce a convective bulk Richardson number Ri of 43, approaching conditions conducive to supercell development (Weisman and Klemp 1984). Conway and Weisman (1988) provide a thorough discussion of the mesoscale environment and storm characteristics observed on this day.

3. Data analysis

a. Polarization measurements

1) Differential reflectivity Z_{DR}

Differential reflectivity has proven valuable in differentiating between regions of surface rain and hail (Aydin et al. 1986). Due to the differences of shapes and fall orientation among hydrometeors, preferred scattering of horizontally (Z_H) or vertically (Z_V) polarized electric fields may exist. A measure of this anisotropy is expressed in terms of the ratio

$$Z_{DR} = 10 \log\left(\frac{Z_H}{Z_V}\right) \quad \text{(dB)}, \qquad (1)$$

where Z_H and Z_V are reflectivity factors (mm^6 m^{-3}) for horizontal and vertical polarization.

Because raindrops larger than 1–2 mm in diameter deform under the influence of aerodynamic forces into oblate spheroids (Pruppacher and Beard 1970), the backscattering of horizontally polarized waves will be stronger, producing positive Z_{DR} values between about 1 and 6 dB in rain regions. Below the melting level in regions containing hail where Z_e (equivalent reflectivity factor) $\geq$ 50 dBZ, Z_{DR} is between about −1 and 1.5 dB. Negative Z_{DR} values are attributed to large (>2 cm) hailstones that are oriented with the major (long) axis in the vertical (Aydin et al. 1990; Balakrishnan and Zrnić 1990). Positive Z_{DR} might be due to smaller hailstones that seem to fall elongated in the horizontal direction, or to simultaneous presence of hailstones and drops in the resolution volume (Meischner et al. 1991; Aydin et al. 1990). Above the melting level, due to random orientation of ice crystals, aggregates, and other ice-phase hydrometeors, $Z_{DR} \approx 0$ dB (Tuttle et al. 1989; Liu and Herzegh 1986; Bringi et al. 1986a); thus, other polarization measurements are needed to determine the presence of hail. Significantly positive Z_{DR} values above the freezing level are likely due to liquid drops.

Figure 4 shows cross sections of Z_e and Z_{DR} through the hailstorm just prior to the dual-Doppler and trajectory analysis time. Whereas Fig. 4b shows the full Z_{DR} field, a threshold of $Z_e \leq 35$ dBZ was used for analysis of polarization data to avoid possible errors due to echoes through sidelobes and sidelobe mismatch (Herzegh and Carbone 1984). These measurement errors, which appear as a false Z_{DR} signature, occur in regions of strong reflectivity gradients such as the vault (at 22-km range, up to 5-km height) or anvil (30-km range, 15-km height). High Z_e and Z_{DR} values of about 0 dB suggest that the surface hail shaft is at 20–22 km in range. The melting level (~2.7 km AGL) and rain region can be seen as the lighter shades between the 10- and 20-km ranges. Note the height variation of the melting layer suggesting larger hydrometeors need longer time to melt and deform, producing the Z_{DR} rain signature (Bringi et al. 1986a). The center of the Z_{DR} column is at a 25-km range and a height of 3 km. About 2 km farther in range is a second column, also coincident with a local increase in reflectivity. It appears this column is supported by the same broad updraft (see Fig. 10). Analysis of the Z_{DR} field within the upper column reveals that values of 1.8 dB extend to 4.0 km.

2) Linear depolarization ratio (LDR)

A cross-polarized power is obtained if a horizontally (vertically) polarized wave is transmitted but vertically (horizontally) polarized echoes are received. The ratio of this cross-polar power (or reflectivity factor) to the power (or reflectivity factor) of copolarized echo (i.e., both transmitted and received waves are horizontally or vertically polarized) defines the linear depolarization ratio

$$\text{LDR} = 10 \log\left(\frac{Z_{HV}}{Z_H}\right) \quad \text{(dB)}. \qquad (2)$$

Here the reflectivity factor for a horizontally transmitted wave is Z_H, and Z_{HV} is the cross-polar reflectivity factor, proportional to the cross-polar returned power; both are obtained at the X-band wavelength.

Attempts have been made to correct the X-band parameters described in the following subsections for attenuation along the propagation path. Because attenuation produces a linear (in decibels) difference between the horizontally polarized S-band (Z_{10}) and X-band (Z_3) signals as a function of range, a piecewise fit of the reflectivity factor difference ($Z_{10} - Z_3$) through a contiguous sequence of radar measurements along each beam can be derived. The measured X-band field is adjusted to this linear fit to yield unattenuated values. The length of the fit varies depending on the reflectivity gradients and is confined to have endpoints between reflectivity minima. LDR is corrected in the same manner except the piecewise fit is through LDR values between minima. As will be seen in the figures that follow, this type of correction does not adequately account for high attenuation encountered in regions of moderate to large hail mixed with rain (Battan and Bohren 1986; Tuttle and Rinehart 1983).

LDR measurements are sensitive to hydrometeor

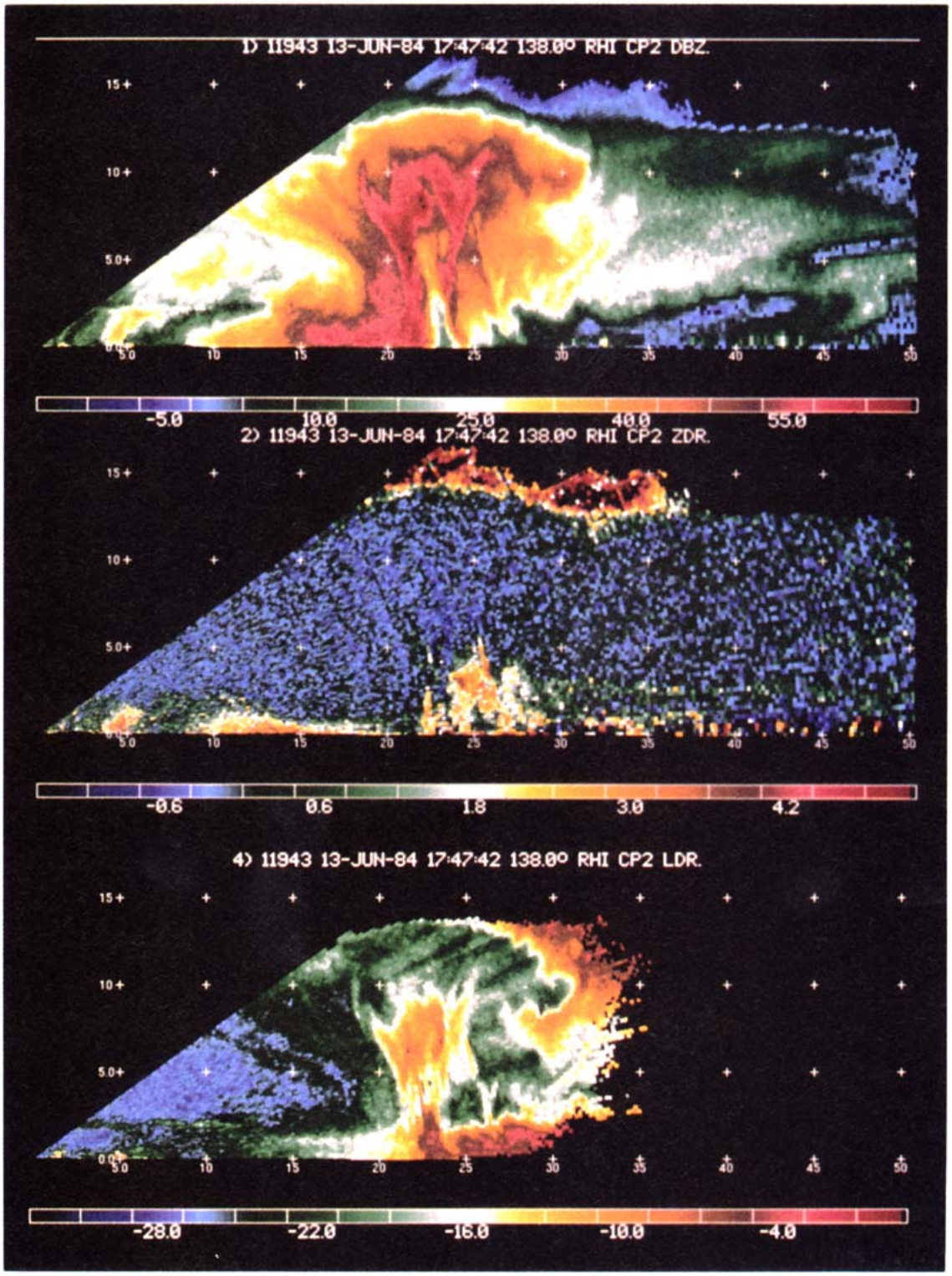

FIG. 4. RHI vertical cross section of (a) reflectivity, (b) Z_{DR}, and (c) LDR (corrected for attenuation) through storm at 1747 LST. Horizontal and vertical scales are in kilometers relative to CP-2 radar location. The surface rain region is centered at about 16 km. The hail shaft (inferred from Z_{DR} of about 0 dB and Z_e greater than about 50 dBZ) is between 19 and 22 km. The differential reflectivity Z_{DR} column is centered at 25-km range and 3-km height. Significant LDR features are low depolarization in the rain (10–17-km range) and the column (25-km range, 4-km height) regions, and high depolarization in the hail shaft.

type, orientation, and dielectric constant. Observations indicate that LDR is −28 to −20 dB in rain where drop canting and deformation are responsible for the larger values (Fig. 4c, 10–17-km range below 2.5 km) (see Herzegh and Jameson 1992; Liu and Herzegh 1986; Bringi et al. 1986a). Locally, high LDRs (−18 to −8 dB) occur throughout the depth of some high-reflectivity cores in thunderstorms. These measurements have been attributed to unaligned, nonspherical hydrometeors that may be in mixed-phase regions (Fig. 4c, 23-km range, 2–9-km height). Low LDR below the freezing level beyond 17 km is due to overestimation of propagation effects (see Herzegh and Jameson 1992). An important observation comes from comparison of Z_{DR} (Fig. 4b) and LDR (Fig. 4c) in the Z_{DR} column region (25-km range, surface to 5-km height). Depolarization in the Z_{DR} column is similar to that of the rain region, suggesting the presence of drops (and possibly spherical or aligned frozen scatterers) above the freezing level coincident with the main updraft.

3) Differential reflectivity hail signal H_{DR}

Aydin et al. (1986) fit a function to the Z_H (in dBZ), Z_{DR} relationship on the boundary of the rain region obtained from disdrometer measurements. This function,

$$f(Z_{DR}) = \begin{cases} 27 \text{ dBZ}, & Z_{DR} < 0 \text{ dB} \\ 19Z_{DR} + 27 \text{ dBZ}, & 0 \leq Z_{DR} \leq 1.74 \text{ dB}, \\ 60 \text{ dBZ}, & Z_{DR} > 1.74 \text{ dB}, \end{cases} \quad (3)$$

represents a rain–hail discrimination envelope. Positive values of H_{DR}, due to hail, are given by the distance of points from the envelope:

$$H_{DR} = Z_H - f(Z_{DR}) \quad \text{(dB)}, \quad (4)$$

where Z_H is in dBZ.

Aydin et al. (1990, 1986) obtained good agreement between positive H_{DR} values and surface hail reports. Above the melting level this parameter detects all forms of ice and cannot be used explicitly as a hail identifier.

4) Dual wavelength hail signal H_{DW}

For hail sizes of about 1 cm, backscattering at a wavelength of 3 cm is in the Mie regime, whereas backscattering at 10-cm wavelength is still Rayleigh; thus, regions where the ratio of the two reflectivity factors is not unity should be an indicator of hydrometeors—particularly hail—greater than about 1 cm in diameter (Atlas and Ludlam 1961). Recalling that the X- and S-band antennas share the same pedestal and have almost equal beamwidths (see Table 1), H_{DW} at each measurement location is given by

$$H_{DW} = 10 \log\left(\frac{Z_{10}}{Z_3}\right) \quad \text{(dB)}, \quad (5)$$

where the attenuation of 3-cm waves is corrected by a procedure described in section 3a.2. Due to uncertainties in the measurements of the two reflectivity factors and slightly different beam patterns (Rinehart and Tuttle 1982), H_{DW} values less than about 6 dB may not be reliable indicators of hail (Herzegh 1990, personal communication). This parameter is particularly useful in hail detection above the freezing level where both Z_{DR} and H_{DR} are ambiguous.

5) Reflectivity difference Z_{DP}

The theoretical percentages of ice and liquid contributions to Z_H within a radar resolution volume are found from the reflectivity difference parameter

$$Z_{DP} = 10 \log(Z_H - Z_V) \text{ (dBZ)}, \text{ for } Z_H > Z_V. \quad (6)$$

Golestani et al. (1989) show that a unique relation (linear on a log–log scale) exists between Z_{DP} and Z_H in rain having a gamma size distribution. Deviations from this relation are attributed to ice hydrometeors and can be used to obtain the fraction of Z_H contributed by ice within the resolution volume. To estimate this linear relation in the current dataset, Z_{DP} versus Z_H was plotted for data in the rain region below the melting level (collected at 1807 LST). Overall, storm intensity had decreased by this time, and bias below the melting level due to ice is assumed to be negligible. Also, only data where $Z_{DR} \geq 1.0$ dB and $Z_H \leq 50$ dBZ were used for the scatter plot (Fig. 5). The least-squares fit line to the points is $Z_{DP} = 1.13Z_H - 9.1$, which is similar

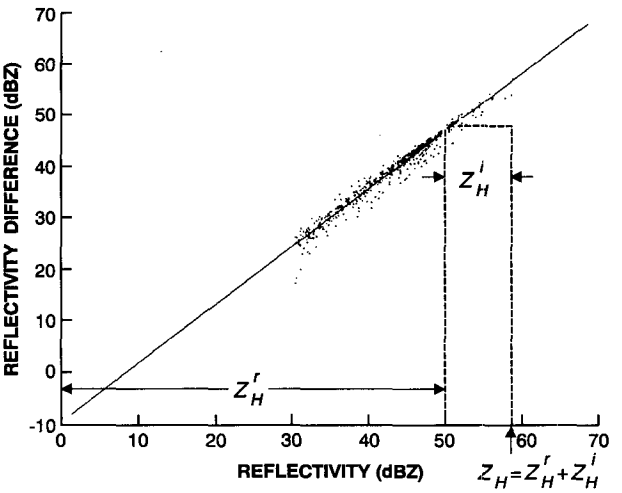

FIG. 5. Scatterplot of reflectivity difference Z_{DP} and reflectivity factor Z_H for 1805 LST below the melting level. The line through the points is a least-squares fit to the data. Superscripts *r* and *i* signify rain and ice, respectively. The distance of points from the line (at constant Z_{DP}) is the contribution to the total Z_H by ice within the radar resolution volume.

to the result of Golestani et al. (1989), who found the slope $m = 1.2$ and intercept $b = -15.8$. The difference could be due to radar calibration inaccuracies or the drop size distributions of the two rain events might have been different. By knowing Z_{DP} and the distance of a point from the rain line, the fraction of reflectivity factor contributed by ice becomes

$$f_i = 1 - \frac{Z^r_H}{Z^r_H + Z^i_H}, \quad (7)$$

where the superscripts r and i signify rain and ice, respectively. This, along with the other available polarization parameters, is used to determine hydrometeor fall speeds and to estimate the contribution of rainlike hydrometeors to the Z_{DR} column. Table 2 summarizes the parameters discussed in the current section.

b. *Dual-Doppler analysis*

Nine volumes of radar data collected throughout the period 1648–1805 LST were available for analysis. Volumes at 1725, 1750, 1800, and 1805 LST were analyzed in detail. The CP-2 scans were collected with beam increments of 1.5° in azimuth and elevation. Two separate autocovariances were estimated from 128 samples each for horizontal and vertical polarizations. Data were recorded from 512 range samples at 200-m spacing. Each volume scan in PPI mode was completed in approximately 4 min. Vertical scans (RHIs) were collected between PPI volumes. The reflectivity factors Z_H and Z_{DR} are thought accurate to within 1 and 0.1 dB (Aydin et al. 1990). Spacing of radial data from the CP-4 radar was about 0.9° and 2.0° in azimuth and elevation. Reflectivity and velocity data were obtained at 512 range locations spaced 160 m apart. Surveillance volumes were completed in about 4.5 min. Radar data were interactively edited to correct for aliased velocities, range ambiguities, ground clutter, sidelobe-induced artifacts, and echoes resulting from forward scattering by hydrometeors to the ground and then back via the hydrometeors to the radar (Zrnić 1987). Editing was performed using the Research Data Support System (RDSS) described by Oye and Carbone (1981). Because the CP-2 radar's unambiguous velocity interval in polarimetric mode was only ±12 m s^{-1}, there were regions in which multiple aliasing occurred. These areas were interactively examined and corrected to preserve local continuity in the longitudinal and transverse beam directions.

The three-dimensional wind field was derived with software developed at the National Severe Storms Laboratory (NSSL) (see Nelson and Brown 1987, 1982). Considering the horizontal and vertical spacing of the collected data, and mean radar to storm distance, interpolation was performed to a grid with spacing of 1.0 and 0.5 km in the horizontal and vertical, using Cressman weighting with a 1.2-km radius of influence.

Vertical velocities w were calculated in the manner suggested by Nelson and Brown (1982). Because the radars did not scan above the storm top, a downward integration of the anelastic mass continuity equation was performed, assuming vertical velocity vanished at the surface and top collection level (12 km) to initially locate major drafts. After the downward integration from 12 km, quadratic profiles were fitted to each major draft, assuming the vertical velocity was 0 m s^{-1} at the storm top. This top was determined to be at 15 km by examining RHI scans and noting where the reflectivity decreased rapidly to less than 0 dBZ. Interpolation of the quadratic fit to 12 km was then made to find the new upper-boundary condition. Final gridded vertical velocities were then derived using a downward integration, and adjusted through redistribution of surface accumulated divergence assuming a constant divergence error with height.

Errors in the derived wind field arise from storm advection, evolution during scanning, incomplete sampling of low-level divergence, top boundary condition specifications, statistical uncertainty in radial velocities, velocity editing procedures, and, especially in this case, uneven terrain features between the radar and storm. Considering these error sources, we estimate the accuracy of horizontal velocity components to be within 2–4 m s^{-1} (Nelson and Brown 1982).

Whereas it is not possible to distinguish individual

TABLE 2. Polarization variables.

Differential reflectivity (dB)	$Z_{DR} = 10 \log\left(\frac{Z_H}{Z_V}\right)$	Depicts water and ice phases and particle shape characteristics.
Linear depolarization ratio (dB)	$LDR = 10 \log\left(\frac{Z_{VH}}{Z_H}\right)$	Responds to particle phase, canting, alignment, and wetting.
Differential reflectivity hail signal (dB)	$H_{DR} = Z_H - f(Z_{DR})$	Discriminates hail below melting layer.
Dual-wavelength hail signal (dB)	$H_{DW} = 10 \log\left(\frac{Z_{10}}{Z_3}\right)$	Discriminates hail above melting layer.
Reflectivity difference parameter (dBZ)	$Z_{DP} = 10 \log(Z_H - Z_V)$	Provides estimates of ice and water contributions to total reflectivity factor.

contributions to the total error field, following Nelson and Brown (1987), errors may be estimated in the vertical velocities by considering the main updraft. Initial accumulated errors (surface residuals) from the downward integration are on the order of 12 m s^{-1}, while the average maximum draft speed is 36 m s^{-1}, giving a maximum error of 33% before redistribution of accumulated divergence. Though this may seem high, experiments with different boundary conditions and integration directions for the vertical velocity calculation show that these errors have few qualitative effects on particle trajectories.

c. *Trajectory calculations*

After inclusion of terminal fall speeds at dual-Doppler grid points (described in the next section), particle trajectory calculations using the derived wind field were done following Brandes (1983). Depending on the number of surrounding grid points, trajectories were determined by interpolating velocity components (u, v, w) to the parcel location using either a linear or second-order Bessel scheme. Each component was then multiplied by a time increment to obtain parcel displacements, after which a forward–backward correction scheme was employed to calculate the final parcel location. If fewer than 64 neighboring grid points were available, interpolation was linear, using one plane above and the other below the parcel location. Otherwise, a second-order Bessel scheme was used for two planes above and two below the parcel. Considering the vertical grid spacing, and maximum updraft velocity of 40 m s^{-1}, a time step of 10 s was implemented for parcel advancement to provide an acceptable truncation error (Ziegler et al. 1983).

d. *Determination of particle fall speeds*

To obtain particle trajectories, hydrometeor fall speeds were subtracted from the Doppler-derived vertical wind field. Based on the reflectivity-weighted fraction of ice and liquid within the radar resolution volume, both mixed-phase and single-phase regions are modeled through a terminal velocity–reflectivity factor relationship. As derived in the Appendix, the mean terminal fall speed $\bar{V}_t$ for hail and/or large graupel is given by[1]

$$\bar{V}_t = 3.95 Z_H^{0.148}. \quad (8)$$

For terminal velocities of raindrops,

$$\bar{V}_t = 2.6 Z_H^{0.107} \quad (9)$$

is used (Atlas et al. 1973).

To apply (8) or (9) in determining terminal fall speeds, Z, Z_{DR}, H_{DR}, and H_{DW} were calculated at each grid point of the Doppler analysis. Because of high X-band attenuation within areas of heavy rain and/or hail, the presence of hail and/or graupel below the melting level was determined from H_{DR}, while above this level H_{DW} was used (see Table 2). Grid points where $Z_e \geq 50$ dBZ were checked for positive hail signatures and/or graupel; if detected, the fraction of ice and water was calculated using Z_{DP} and (7). The terminal fall speeds assigned to those grid points is given by

$$\bar{V}_t = 2.6 f_r (f_r Z_H)^{0.107} + 3.95 f_i (K f_i Z_H)^{0.148}. \quad (10)$$

Here K depends on the complex refractive indices of water and ice, and takes into account the change in dielectric constant due to the presence of dry and/or water-coated hailstones. From the LDR signatures found in the core of this storm (see Fig. 4c) it is assumed that dry and wet hail may exist above the freezing level where K is set to 3.15, halfway between the values of ice (5.3 at a density of 0.9 g cm^{-3}) and water (1.0) (Doviak and Zrnić 1984). It is assumed that, below the height of 3 km, hail has a water coating, and there K is set to 1.0. This would produce a maximum error in terminal fall speeds of about 3 m s^{-1} in the unlikely event of only dry hail below 3 km.

As shown by Pflaum et al. (1982) and Ziegler et al. (1983), hailstone growth and, consequently, fall speeds and trajectories are affected by embryo and hailstone density variations. But K is not significantly affected, because over the range of densities 0.22–0.91 g cm^{-3} it varies by less than 2% (Battan 1973). Thus, for this application, density variations are not a significant source of error.

Figure 6 shows the H_{DR} and H_{DW} fields for the range–height indicator (RHI) scan in Fig. 4. The differential reflectivity hail signal H_{DR} exhibits a smooth transition through the hail shaft to the back edge of the storm below the melting level. In contrast, heavy attenuation below the melting level has produced a notch in H_{DW} at a range of 24 km; beyond, the high H_{DW} signature is from undercorrection of X-band attenuation. Above the melting level, higher H_{DR} values are consistent with the reflectivity pattern in areas such as the vault and main core. Although attenuation is a factor beyond 27 km in range at a 10-km height, only (9) is used to calculate $\bar{V}_t$ as $Z_e < 50$ dBZ in this region.

The results of the terminal fall-speed algorithm are in Fig. 7. Areas with maximum hail sizes without corresponding fall-speed maxima also contain rain; thus, the weighting by f_r in (10) reduces the average fall speed. Maximum fall speeds (~33 m s^{-1}) and hail sizes (~8-cm diameter) correspond to regions of highest Z_H, there raindrops contribute least to $\bar{V}_t$. Hail sizes were derived using (A10). NWS spotters reported hail sizes of up to 6-cm diameter at this time. This corresponds well with the surface hail sizes shown in Fig. 7b. The hail swath (determined by hailstones diameters exceeding 2 cm) is broader at the ground than aloft.

[1] Here Z_H (mm^6 m^{-3}) is used in place of Z [see (A11)] to emphasize that horizontal polarization is considered.

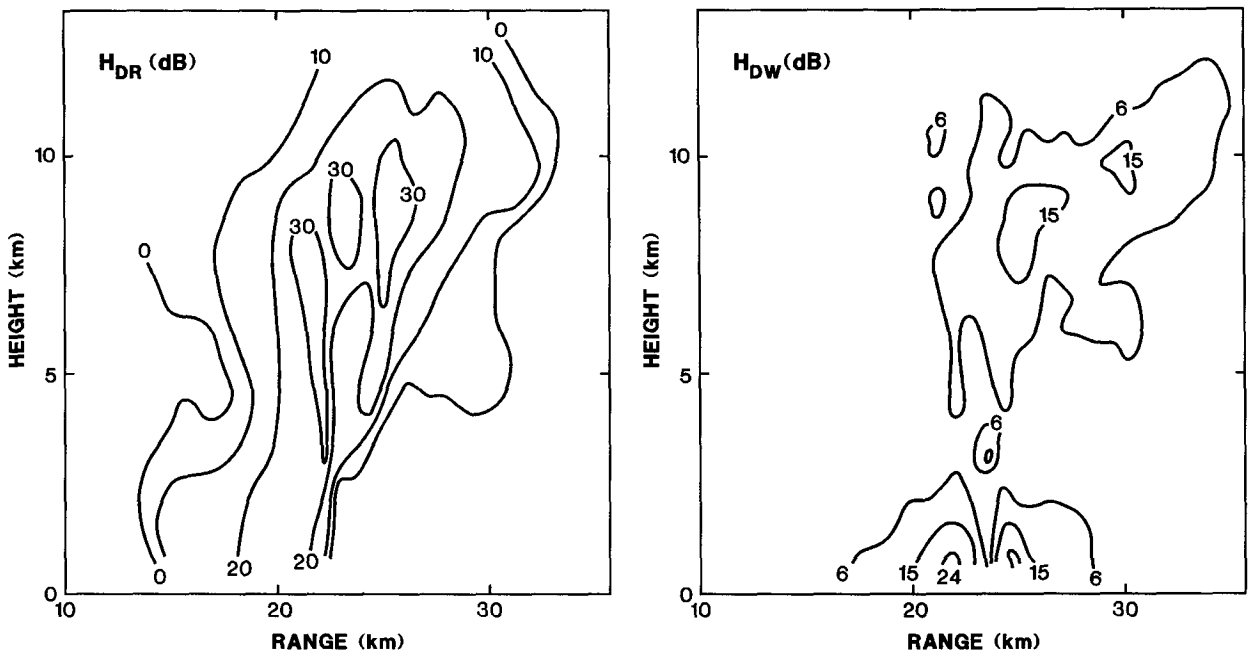

FIG. 6. RHI vertical cross section for the same time as in Fig. 4, depicting (a) H_{DR} and (b) H_{DW}. Contours of H_{DR} are in 10-dB increments. The dual wavelength hail signal H_{DW} is contoured at 6, 15, and 24 dB.

This is partly due to downdraft spreading and to trajectories that are in and out of the plane in Fig. 7b (see section 4).

Figure 8 summarizes the particle trajectory calculation. At each grid point, the radar parameters were examined to determine the presence (or absence) of ice. If ice was present (or absent), (10) [or (9)] was used to assign a terminal fall speed to the grid point. These fall speeds were subtracted from the vertical velocity field before performing trajectory calculations.

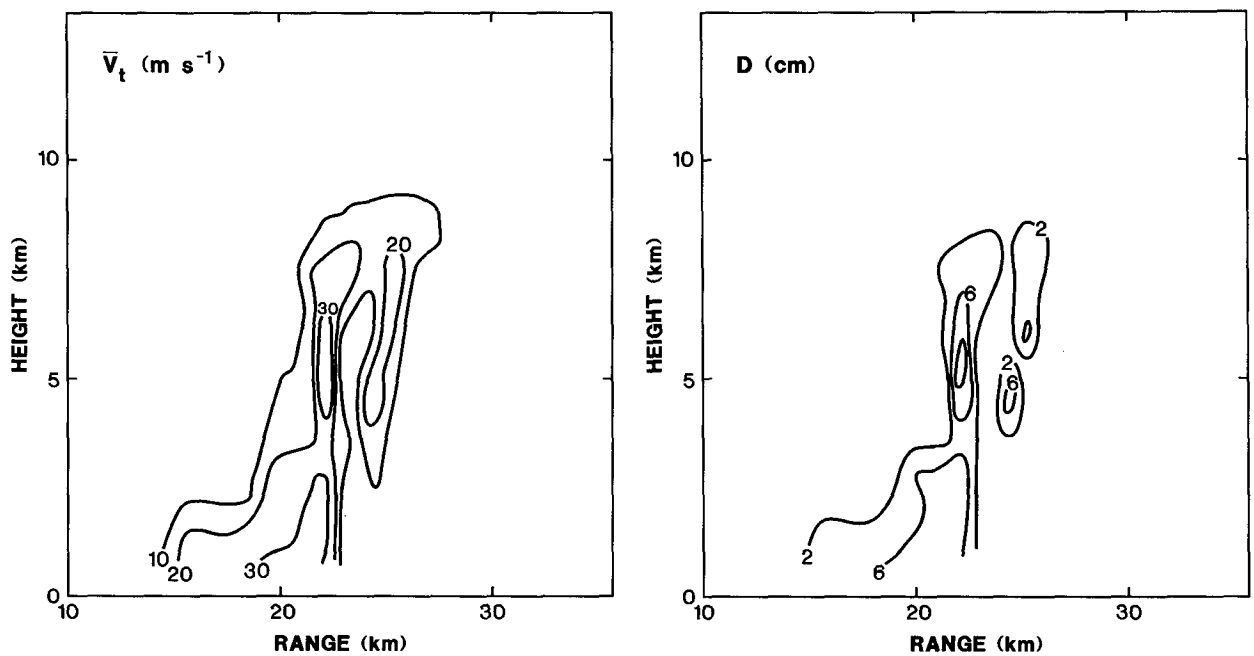

FIG. 7. Same as Fig. 6 except (a) terminal fall speeds, derived from Eq. (A10), contoured in 10 m s^{-1} intervals and (b) hail sizes contoured in increments of equivalent volume diameter D; the contour at range 22 km and height 6 km is for D = 8 cm.

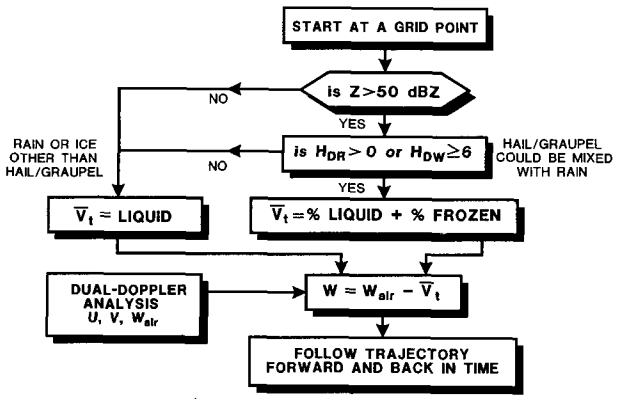

FIG. 8. Flowchart of the algorithm to estimate terminal fall speeds.

Whereas this procedure assigns a bulk fall speed to the grid points, mean speeds for the ice and liquid portions of hydrometeors are different. A more sophisticated approach to trajectory determination would involve separation of liquid from frozen constituent at each point, and track each separately. Such analysis was deemed unnecessary, as trajectory experiments using only (9) instead of (10), below the melting level (where $Z_e \geq 50$ dBZ), showed little difference in trajectory paths.

4. Results

Because the wind fields from four consecutive dual-Doppler analysis are similar, we suggest that the storm was in a quasi-steady state. Furthermore, hydrometeor trajectories are similar for these four volumes. The reflectivity field was also in a quasi-steady state as expected, considering that the microphysical processes are directly related to the kinematic field. The data at 1750 LST was chosen for detailed analysis because at that time scanning was best correlated between the radars.

a. Dual-Doppler analysis

Dual-Doppler analysis at a height of 3.5 km AGL, about 800 m above the melting level (Fig. 9a), reveals cyclonic curvature in the updraft region corresponding to the reflectivity notch and inflow area. Sector limits were such that wind retrieval in the southwestern edge of the domain is not possible. One broad updraft dominates the storm structure, but two downdraft centers are apparent in Fig. 9b. A collocation of the Z_{DR} column and the main updraft is evident, whereas the Z_{DR} field is about 0 dB elsewhere above the melting level; the Z_{DR} column is offset northwest of the updraft's center, suggesting large drops are not in the weak reflectivity notch (vault). This is consistent with previous studies (e.g., Browning and Foote 1976) that propose that hydrometeors in updraft centers are swept into the upper part of the storm too quickly for in situ growth; thus, the weak echo vault is created.

Figure 10 depicts scatter plots of Z_{DP} and Z_{DR} versus Z_H above the melting level within the Z_{DR} column. The scattergram in Fig. 10b is from direct measurement, whereas the scattergram in Fig. 10c has been

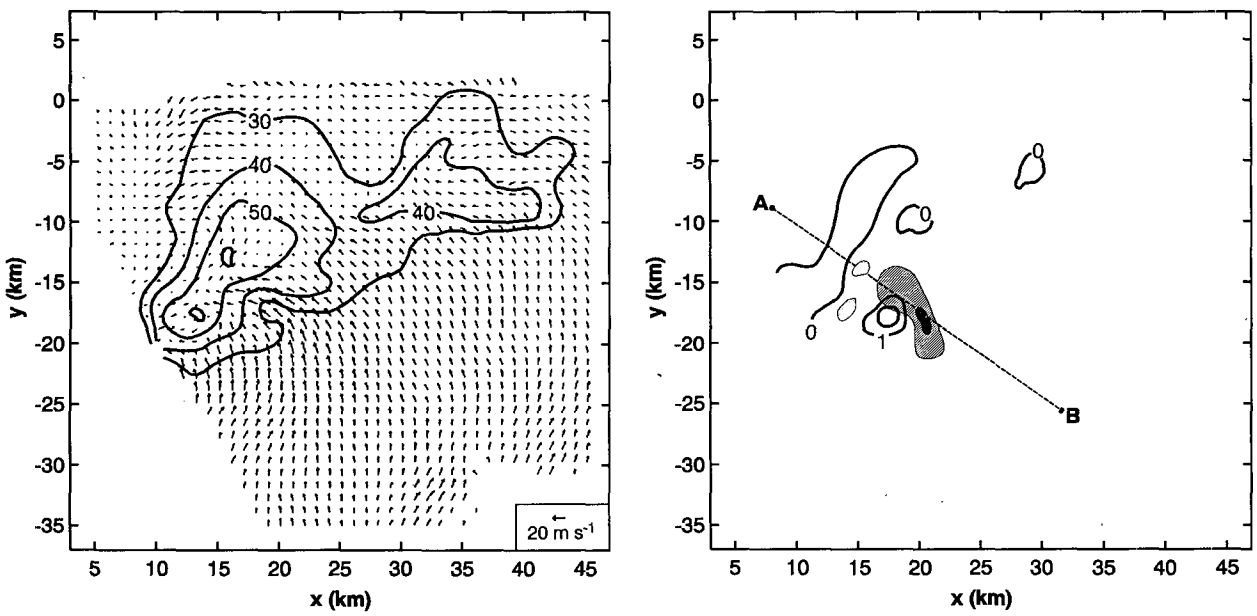

FIG. 9. Analyzed reflectivity and velocity fields at 3.5 km AGL (800 m above freezing level). (a) Storm relative flow field and reflectivity field contoured in 10-dB increments. Distances x (west to east) and y are with respect to the CP-2 radar. In (b), Z_{DR} contours are in 1-dB increments. The column is on the northwest flank of the updraft. Light hatching represents updraft velocities $w \geq 10$ m s^{-1}. Dark hatching is for $w \geq 15$ m s^{-1}. Downdrafts stronger than -5 m s^{-1} are shaded. Note location of updraft in the reflectivity notch (see Fig. 9a). Line *AB* locates the cross section shown in Fig. 11.

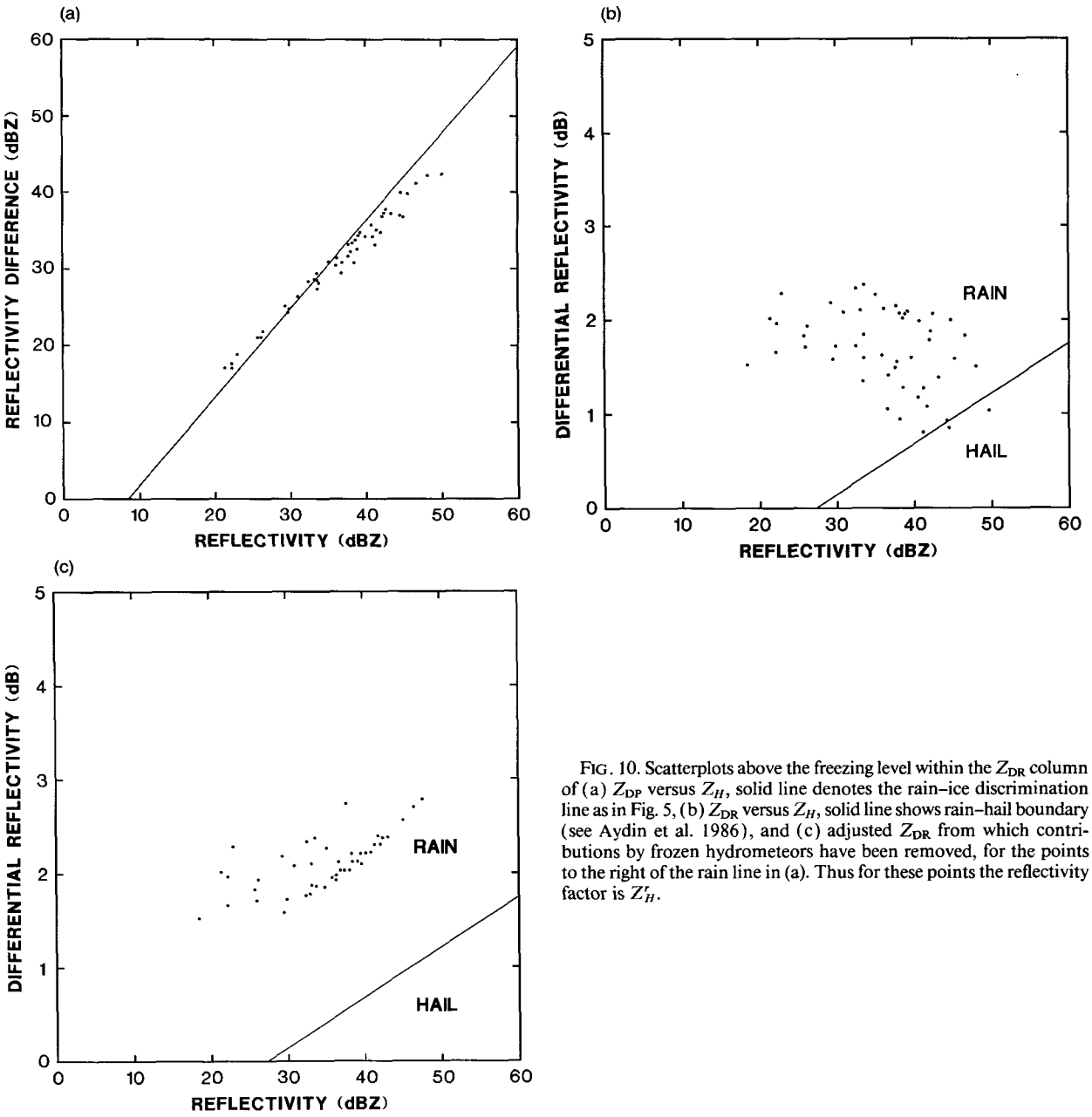

FIG. 10. Scatterplots above the freezing level within the Z_{DR} column of (a) Z_{DP} versus Z_H, solid line denotes the rain–ice discrimination line as in Fig. 5, (b) Z_{DR} versus Z_H, solid line shows rain–hail boundary (see Aydin et al. 1986), and (c) adjusted Z_{DR} from which contributions by frozen hydrometeors have been removed, for the points to the right of the rain line in (a). Thus for these points the reflectivity factor is Z'_H.

obtained from data in Fig. 10b after removing the contribution of ice hydrometeors to the reflectivity factors Z_H (horizontal polarization) and Z_V (vertical polarization). This removal is accomplished by using the reflectivity difference to estimate the contribution by ice, as in (7), and by adjusting the Z_{DR} values accordingly. The scattergram in Fig. 10c is similar in shape to a scattergram presented by Leitao and Watson (1984) for data from rain, and to a scattergram from simulations by Meischner et al. (1991), but our scattergram has higher Z_{DR} values; that is, it is shifted by about 0.5 dB! The presence of wet ice structures and drops with ice cores in addition to raindrops can explain the observed scattergram. We estimate the average[2] Z_{DR} to be 2.2 dB, to which corresponds a median (equivalent volume) "drop" diameter D_0 of 2.8 mm. Because the scattergram (Fig. 10c) indicates that there is a distribution of hydrometeor sizes [Z_{DR} from 1.5 to 2.9 dB would correspond to D_0 from 1.9 to 3.6 mm, if drops had an equilibrium shape, Pruppacher and Beard (1970)], we speculate that the largest

[2] Adjusted and nonadjusted points from Fig. 11c have been included in the calculations of the averages.

[3] Henceforth "drops" will be used to designate mixture of raindrops and wet oblate hydrometeors, including drops with ice cores, all of which we believe coexisted in the column.

"drops"[3] are likely supported by ice cores, or they might be partially melted ice structures that are oblate and horizontally oriented, as described by Rasmussen and Heymsfield (1987a). Examination of the reflectivity factors reveals that the average values in the column are Z_H^r = 35 dBZ and Z_H^i = 33 dBZ; thus, if hydrometeors that scatter like liquid water have large diameters, they should be sparse. On the other hand, the wet ice structures might be small (<3 mm) and more numerous but with axis ratios larger than expected for drops. In summary, it seems likely that the column consists of drops, ice cores surrounded by water, wet oblate structures, and approximately spherical ice particles. As will be shown later, this ice is likely small hail (or graupel) that crosses the column and grows within it.

Our adjusted Z_{DR} values are lower than previous observations of Z_{DR} columns that contained values of up to 5 or 6 dB (above the melting level) that were attributed to small concentrations of large (5–6 mm) drops, but the origins of these drops and our "drops" are different. These columns are thought to be formed by the collision–coalescence process, or melting of ice of an unknown origin (Meischner et al. 1991; Tuttle et al. 1989; Caylor and Illingworth 1987). Our value of average D_0 corresponds to drops with fall speeds (6–9 m s^{-1}) on the order of updraft speeds found northwest off the main updraft axis. As this is a median fall speed, some drops would have been advected upward while others would have fallen through this updraft.

Figure 11 shows a vertical cross section along line *AB* in Fig. 9. The overhang and vault regions are apparent, and the embryo curtain extends down to the melting level at about 3 km AGL (at a 20-km range). One important feature of the flow field is the horizontal circulation centered at a distance of 24 km and 9-km height. This circulation indicates that some particles might fall from the back-sheared anvil into the embryo curtain where they could melt and then be recaptured by the updraft to become frozen drop embryos. Graupel particles that do not fall below the melting level may also be recirculated as embryos. These hypotheses are detailed in the following subsections.

b. *Trajectory analysis*

Presented now are trajectories to determine possible origins of the Z_{DR} column and hail-fall regions, and the relation between the two. Because hail fell in two distinct areas, these northern and southern hail-fall regions are presented separately. In the figures showing hailstone trajectories, H_{DW} values are indicated along the hailstone paths to infer hail growth. Final values at the surface have a large bias due to X-band attenuation below the melting level, and are not intended to suggest substantial growth below the melting level. All references to LWC or temperature values are derived from the sounding in Fig. 3.

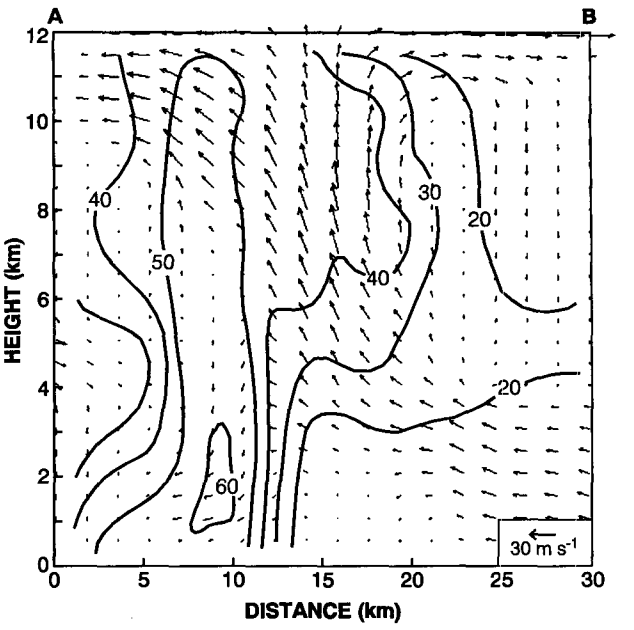

FIG. 11. Cross section along line *AB* in Fig. 9. The reflectivity factor contours are in dBZ. Distance is along line *AB*. Note the vault at 15 km and overhang at about 18 km. The circulation centered at a distance of 21 km and 9 km in height carries hydrometeors from the back-shear anvil into the main updraft.

1) Z_{DR} COLUMN ORIGIN

After examining some 80 trajectories, we concluded that three main trajectories account for the majority of paths that start at different locations within the Z_{DR} column (Figs. 12 and 13). Note that the vertical cross sections through the storm are chosen to contain a large portion of the trajectory, and cut the Z_{DR} column as well. All trajectories originate from the southwestern edge of the domain and fall cyclonically toward the reflectivity overhang, as seen in Fig. 12. Hydrometeors falling below the melting level produce an increase in Z_{DR} as they melt. Some particles that enter the column at heights where their terminal fall speeds are less than the updraft are carried away into the forward anvil region (path A).

As stated previously, due to scan limitation, the full wind field in the vertical cross section within the southwestern region of the storm is not retrievable. Considering the cross section in Fig. 11, the conceptual model of recirculation in Fig. 1, and the trajectory origins and paths in Figs. 12 and 13, we suggest that similar recirculation, as shown by the dashed line from path A (Fig. 13), might also occur. Thus, it is possible that a circulation exists on the southwest flank of the storm. In that case some hydrometeors of the Z_{DR} column could be circulated through the back-shear anvil and fall cyclonically into the plane shown in Fig. 13. Because path A does not descend below the melting level, it might contain graupel hailstone embryos (i.e., the ones that contributed to the ice fraction of the reflectivity factors).

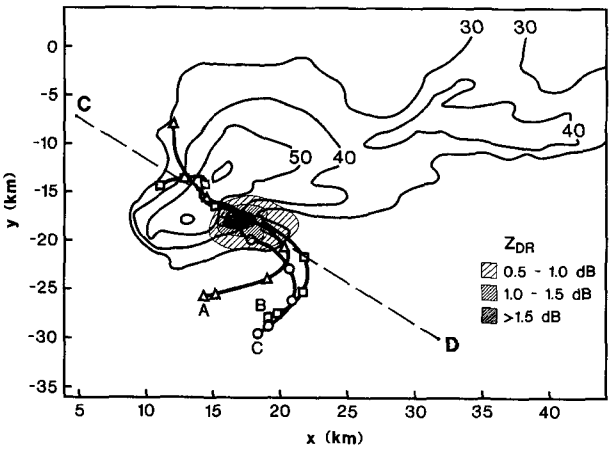

FIG. 12. Projection at 3.5 km AGL of three main trajectories that pass through the Z_{DR} column region. The reflectivity contours are 10 dB apart. The differential reflectivity Z_{DR} values are hatched in 0.5-dB increments. Coordinates x and y are relative to the CP-2 radar. Markers along trajectories indicate 4-min time increments. Path A leads into forward anvil, B ends in rain, and C leads into the southwestern rain region.

The second trajectory (B) shows hydrometeors falling from the back-shear anvil, melting, and entering the updraft. Upon entering the updraft, hydrometeors rise above the freezing level and fall out as rain (path B), or might serve as frozen drop embryos (heavy dashed line from path B). This path is inferred using the same argument as in the previous paragraph.

A third trajectory, in which particle fall speeds are greater than the updraft at their entrance points, continues through the column and ends in surface rain (path C). This path seems to coincide with the juxtaposition of the lower-level cyclonic flow field and the melting layer.

Trajectory types A and B have been modeled by Miller et al. (1988), who show that graupel 2–3 mm in diameter falls from the back-shear anvil and into the main updraft. Hail collection occurred at 1730 LST in the southwestern part of the storm domain. According to N. Knight (1989, personal communication), the majority of hailstones contained frozen drop embryos 2–3 mm in diameter. Given our mean value of $D_0 = 2.8$ mm and the fact that these drops probably contained ice cores, it is reasonable to expect that liquid drops had smaller diameters. Thus, these smaller drops from the Z_{DR} column could have been recirculated by the flow field to become frozen drop embryos.

2) NORTHERN HAIL-SHAFT TRAJECTORIES

Surface grid points of high Z_H (>50 dBZ), low Z_{DR} (<0.5 dB), and positive H_{DR} are deduced to be hail fallout locations. Trajectory analysis was performed on all grid points where hail was thought to reach the surface. The analysis yielded two main trajectories for the northern hail-fall location (Figs. 14, 15, and 16).

Trajectory A (Fig. 14) originates directly from the ambient inflow region and passes through the main updraft and eastern portion of the column edge. This trajectory type has been modeled by Danielsen et al. (1972) for broad initial drop spectra where frozen drop embryos can grow entirely within the updraft. The stochastic collection process accounts for the initial formation of drops that freeze and then rapidly collect supercooled droplets. Foote (1985) suggested that the continental initial drop spectrum of Colorado clouds (a lower concentration of smaller drops with an absence of large drops) does not allow enough time for the coalescence process to occur within an average updraft. Nevertheless, the presence of larger drops, as depicted by the Z_{DR} column, might indicate a localized, broad initial spectrum of sizes. In addition, according to Danielsen et al. (1972), the approximate 6-min period that hydrometeors spend along path A in the column–updraft region is long enough for hail growth to occur. Furthermore, H_{DW} increases significantly through the column, above the freezing level (see Fig. 15a), and then into the high-reflectivity core, suggesting rapid growth at cloud temperatures of −5° to −18°C, and LWC of about 4–6 g m^{-3}. This type of growth has also been observed by Tuttle et al. (1989) in a southern plains storm.

Path B (Fig. 14) is typical of the majority of trajectories that pass over the vault encountering colder temperatures (−20° to −30°C) and lower LWC (1–3 g m^{-3}). Again, a substantial increase of H_{DW} occurs as the trajectory crosses the vault (see Fig. 15b). Because the Z_{DR} column does not extend to the top of the vault, we conclude that large supercooled drops are absent, but supercooled droplets might exist at this height, aid-

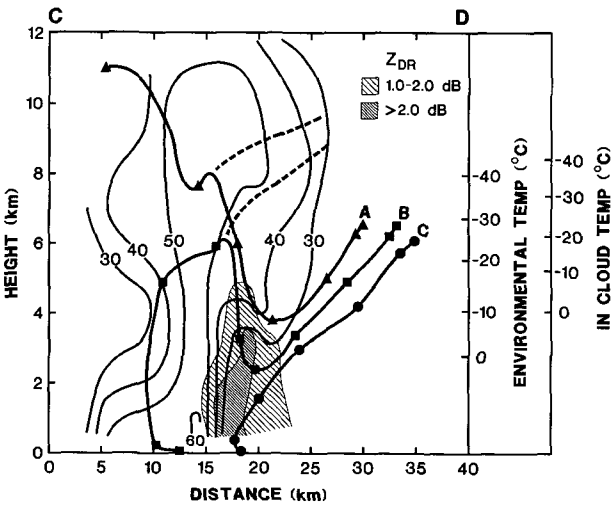

FIG. 13. Cross section along CD in Fig. 12. The reflectivity is contoured as in Fig. 12, and the column is hatched at 1.0-dB increments. Environmental temperature is on the left vertical axis; cloud relative temperatures are indicated on the right vertical axis. Heavy dashed lines represent possible recycling paths, as inferred from the reflectivity bulge at a distance of 25 km and height of 11 km.

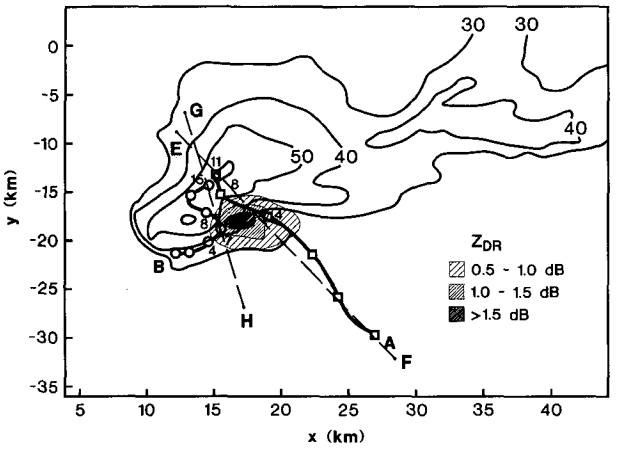

FIG. 14. Same as Fig. 12 except trajectories are for hail paths that end in the northern hail-fall region. Values of H_{DW} (dB) are plotted along hailstone paths. Path A originates in the ambient inflow and passes through the column. Path B descends from the overhang region and rises across the top of vault (Fig. 15b). Note a substantial increase in H_{DW} as trajectories cross the Z_{DR} column.

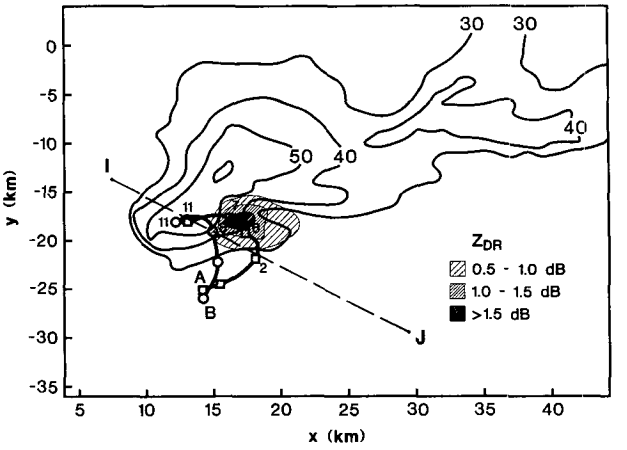

FIG. 16. Same as Fig. 14 except for hail fall that ends in the southern region. Path A crosses directly through drop column, while B crosses the south edge of the column.

ing in hail growth. The embryo origin for this path could be frozen drops that have recycled into the updraft, grown during ascent (increasing their fall speed), and fallen into the midlevel streamflow where they are carried across the vault in an anticyclonic path similar to that discussed by Miller et al. (1990) and Bluestein and Woodall (1990) (see Fig. 1, path B).

3) SOUTHERN HAIL-SHAFT TRAJECTORIES

Two main trajectories exist for surface hail fall in the southern region (Figs. 16 and 17). Both paths imply that particles fall cyclonically from the southern flank of the storm. Trajectory A passes above the Z_{DR} column where temperatures and LWC are estimated to be $-8°$ to $-10°$C and 4–5 g m^{-3}. Trajectory B passes over the southwestern updraft flank, encountering temperatures of $-10°$ to $-20°$C and LWC of 2–4 g m^{-3}. Both trajectories show a H_{DW} increase, and resemble paths described by Miller et al. (1990); that is, they acquire cyclonic curvature and end in the southwestern region of the storm (see also Fig. 1, path C). Calculations indicate that this is a fallout area of largest (6 cm) hail. It could be that this maximum size resulted from the growth environment of trajectory B in which the range of temperatures and LWC are consistent with modeling results (Nelson 1983) and observations (Knight and English 1983) for largest hail growth.

Recall that hail collection in proximity to trajectories A and B yielded hailstones with frozen drop embryos.

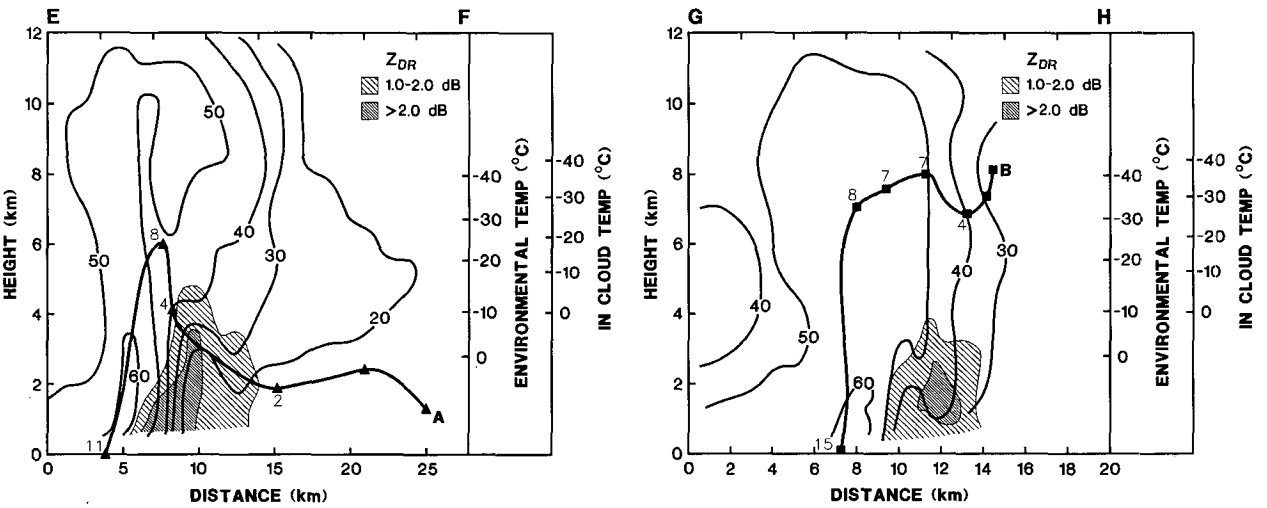

FIG. 15. Cross sections from Fig. 14 along (a) line *EF* showing path A and (b) line *GH* showing path B. Reflectivity and Z_{DR} are contoured as in Fig. 13. The dual wavelength hail signal H_{DW} is indicated along trajectories as in Fig. 14.

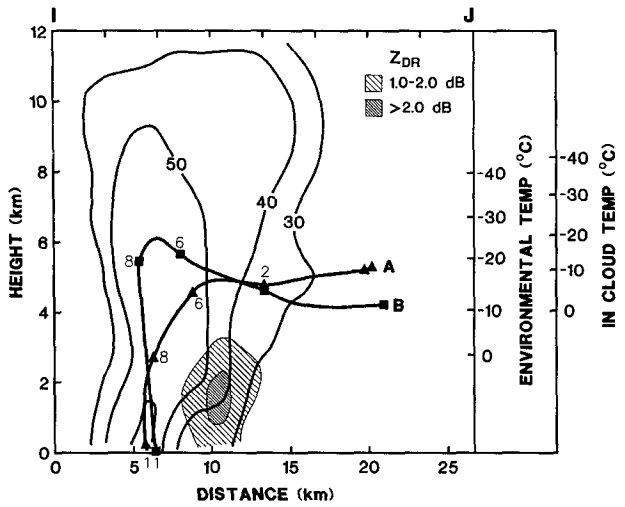

FIG. 17. Cross section along line *IJ* in Fig. 16. Contours are as in Fig. 13, and H_{DW} is plotted as in Fig. 14.

As neither path of the southern fallout region crosses the melting level, the source of the drop embryos must be elsewhere. One explanation is that drops from the Z_{DR} column freeze in the updraft and recirculate through the back-shear anvil, the mid to upper embryo curtain, and then grow to hail size in a final pass across the column.

5. Summary

The purpose of this study is to relate the microphysical processes in a severe hailstorm to its kinematic fields. Dual-Doppler analysis together with polarimetric and dual-wavelength measurements were used to accomplish this goal. Polarization and dual-wavelength variables provided identification of regions with rain, hail, or mixed phase, allowing estimation of the fall velocities of these hydrometeors. Dual-Doppler analysis and the terminal fall speeds were used to reconstruct particle trajectories within the storm. Of particular significance is the discovery of a column of positive differential reflectivity that extended well above the freezing level. Using the reflectivity difference, we were able to separate the contributions to the reflectivity factors (in the column) by drops and wet particles from the contributions by frozen, approximately spherical hydrometeors. Thus, we have adjusted the Z_{DR} values to reflect contributions of the former hydrometeors. The Z_{DR} column had an important role in embryo production and hail growth. Principal findings concerning the column and hail formation are as follows.

The column consisted of drops of oblate wet hydrometeors and of approximately spherical frozen hydrometeors. The "drops" (drops and wet hydrometeors) had a median diameter of 2.8 mm and extended to about 2 km above the freezing level. The column was offset (northwest) from the storm's updraft center and the weak reflectivity notch (vault), suggesting that hydrometeors in the center were swept into the upper part of the storm too quickly for in situ growth of hailstones. The Z_{DR} column coincided with weaker updraft that provided support for sizable drops (both liquid and with ice cores), leading to the possibility of in situ hail growth.

Hydrometeors forming the column originated in the southwestern part of the storm and fell cyclonically through the reflectivity overhang. Some trajectories carried particles to the downwind anvil and out of the storm. Others contained hydrometeors that fell as rain, and still others might have recirculated particles to serve as frozen drop hailstone embryos. The origin of the drops responsible for the Z_{DR} column appears to be ice hydrometeors that fell from the back-sheared anvil and melted.

Trajectory analysis suggests the lowest part of the column, below the melting level, is caused by the proximity of the melting level to the low-level cyclonic flow. Frozen hydrometeors descend, melt, and are caught by the cyclonic airflow and carried into the updraft. Because their terminal velocities are greater than updraft velocities, they continue to descend below the melting level and reach the surface as rain. Above the freezing level, the column consists of melted, partially melted, and frozen hydrometeors that have entered the updraft at altitudes where their fall speeds do not exceed the updraft velocities. These hydrometeors are then advected upward on the western updraft flank.

Two more sources of embryos are likely. Hydrometeors that enter the updraft region above the melting layer may serve as graupel embryos. An additional source, which could not be confirmed in this study, is shedding of drops that collect on hailstone surfaces during wet growth or that are shed during melting as they pass through the column (Rasmussen and Heymsfield 1987b). These shed drops could then be advected above the freezing level, and their contribution to Z_{DR} would become secondary to the contribution by the column drops that originated elsewhere. Nevertheless, polarimetric measurements and trajectories do indicate that the majority of frozen drop embryos originate above the freezing level in the back-shear anvil.

Two distinct hail fallout regions (northern and southern) were found. In the northern fallout area, growth was either from "scratch," where most mass was acquired as embryos crossed the column, or embryos grew as they were carried over the vault. These anticyclonic trajectories are similar to those reported by Miller et al. (1990) and Bluestein and Woodall (1990). Southern hailstone paths descended cyclonically from the same southwestern part of the storm as hydrometeors that formed the Z_{DR} column. These hailstones either fell through the column where they acquired the majority of their mass, or passed through the vault, again along paths similar to trajectories discussed by Miller et al. (1990). These particular frozen drop embryo trajectories represent a full recirculation

path. Their origin is drops in the Z_{DR} column that freeze, enter the back-shear anvil, fall but stay above the melting level, and then cross the column acquiring the mass needed to attain hail size. Although it is not known if embryos undergo multiple column-to-anvil recirculation as they pass through the melting level, it appears that they attain hail size in a single crossing of the updraft–column region.

There are distinct differences between the Z_{DR} column reported in this and other works. The columns observed in the United States southern plains, England, and Germany are thought to be formed mainly through the collision–coalescence rain process (Meishner et al. 1991; Tuttle et al. 1989; Illingworth et al. 1987). This produces high Z_{DR} values of up to 4–6 dB above the freezing level, corresponding to the presence of a small concentration of large drops. In our observations the measured Z_{DR} is low because of the presence of frozen, partially melted, and liquid hydrometeors. After removing the frozen hydrometeor contribution to the reflectivity factors we obtain Z_{DR} values from 1.5 to 3 dB. Thus, the residual hydrometeors are deduced (from adjusted Z_{DR}) to be drops and wet oblate particles. Hence, collision–coalescence is secondary to melting of frozen hydrometeors, although it plays a primary role in hail formation for some trajectories. On the other hand, columns with high (not adjusted) Z_{DR} values are found in geographical regions with large LWC at low altitudes, resulting in more efficient collision–coalescence. Particle melting is likely present but less important.

We suggest that hailstorms in the High Plains that do not contain frozen drop embryos will have a far less pronounced Z_{DR} column. These would be storms in which the reflectivity overhang does not extend below the melting level, leaving collision–coalescence the only column-producing mechanism available. An abundance of graupel embryos should be present, as frozen drop recycling would not be possible. On the other hand, if shedding is the primary source of the Z_{DR} column, then columns should be frequent and would be part of storms whose overhang remains above the melting layer.

Overall, the Z_{DR} column seems important in both embryo production and the hail-growth process. Future work should include a Z_{DR} column "climatology" to examine its occurrence within different geographical locations, mesoscale environments, and storm types.

Acknowledgments. This work evolved from an M.S. thesis done at the University of Oklahoma. Paul Herzegh provided the initial incentive for this research and helped greatly in its evolution. Ed Brandes wrote the trajectory analysis software and provided useful advice. Other committee members, Howard Bluestein and Kelvin Droegemeier, supplied avid discussions and thesis reviews. Kevin Thomas helped explore the dual-Doppler software. Art Jameson provided the X-band correction software, and Joan Kimpel drafted many of the figures. Nancy Knight took time to do hailstone cross sections for this study. Useful reviews of the paper were made by Conrad Ziegler and Bill Martin. Finally, three anonymous reviewers provided exceptionally constructive comments. Part of the research was supported by a grant from the National Severe Storms Laboratory to the Cooperative Institute for Mesoscale Meteorological Studies at the University of Oklahoma.

APPENDIX

Hail Terminal Velocities

A power law of the form

$$V_t = aD^b \quad (\mathrm{m\ s^{-1}}) \tag{A1}$$

is assumed as an analytical solution for fall speeds V_t, where D is the hydrometeor diameter, and a and b are constants determined by observations (Atlas et al. 1973). The purpose here is to retrieve these constants and derive a form of V_t as a function of the reflectivity factor Z.

Consider the mean velocity $\bar{V}_t$ as defined by the first moment of the Doppler spectrum $S(v)$ obtained with a radar at vertical incidence

$$\bar{V}_t = \frac{\int_0^\infty vS(v)dv}{\int_0^\infty S(v)dv} = \int_0^\infty vS_n(v)dv. \tag{A2}$$

The reflectivity factor is related to the normalized Doppler spectrum $S_n(v)$ and hydrometeor size distribution $N(D)$ by

$$ZS_n(v)dv = D^6N(D)dD, \tag{A3}$$

where

$$Z = \int_0^\infty N(D)D^6dD \quad (\mathrm{mm^6\ m^{-3}}). \tag{A4}$$

Here $N(D)$ is assumed exponential; that is, $N(D) = N_0e^{-\Lambda D}$, where N_0 is the hydrometeor concentration ($\mathrm{m^{-3}\ mm^{-1}}$) and Λ ($\mathrm{mm^{-1}}$) is the slope parameter. Substitution of (A1) and (A3) into (A2) and integration yields the mean terminal fall speed $\bar{V}_t$

$$\begin{aligned}\bar{V}_t &= \frac{\int_0^\infty aN_0e^{-\Lambda D}D^{(6+b)}dD}{\int_0^\infty N_0e^{-\Lambda D}D^6dD} \\ &= \frac{aN_0\Lambda^7\Gamma(7+b)}{N_0\Lambda^{(7+b)}\Gamma(7)} \\ &= \frac{a\Gamma(7+b)}{\Lambda^b\Gamma(7)}.\end{aligned} \tag{A5}$$

Using observations from 41 hailstone distributions in seven Alberta storms, Cheng and English (1983) found the best fit for the size distribution to be

$$N(D) = 115\Lambda^{3.63}e^{-\Lambda D} \quad (\mathrm{m^{-3}\ mm^{-1}}). \tag{A6}$$

Substituting this result into (A4) and integrating gives

$$Z = \frac{115\Lambda^{3.63}\Gamma(7)}{\Lambda^7}, \quad \text{(A7)}$$

or in terms of the slope parameter

$$\Lambda^{3.37} = \frac{115\Gamma(7)}{Z}. \quad \text{(A8)}$$

Substitution of (A8) into (A5) gives

$$\bar{V}_t = a\left[\frac{115\Gamma(7)}{Z}\right]^{-b/3.37}\frac{\Gamma(7+b)}{\Gamma(7)}. \quad \text{(A9)}$$

Matson and Huggins (1980) compared theoretical and empirical expressions for terminal fall speeds of hailstones to their own data measured in several Colorado storms. They found the best fit of terminal velocity to hailstone diameter (mm) to be

$$V_t = 3.62\sqrt{D} \quad (\text{m s}^{-1}). \quad \text{(A10)}$$

Using these values of $a = 3.62$ and $b = 0.5$ in (A9) gives the final form of the desired relationship for terminal fall speeds of hail and/or larger graupel

$$\bar{V}_t = 3.95Z^{0.148}. \quad \text{(A11)}$$

REFERENCES

Atlas, D., and F. H. Ludlam, 1961: Multi-wavelength radar reflectivity of hailstorms. *Quart. J. Roy. Meteor. Soc.*, **87,** 523–534.

——, R. C. Srivastava, and R. S. Sekhon, 1973: Doppler radar characteristics of precipitation at vertical incidence. *Rev. Geophys. Space Phys.*, **2,** 1–35.

Aydin, K., T. A. Seliga, and V. Balaji, 1986: Remote sensing of hail with a dual linear polarization radar. *J. Climate Appl. Meteor.*, **25,** 1475–1484.

——, Y. Zhao, and T. A. Seliga, 1990: A differential reflectivity radar hail measurement technique: Observations during the Denver hailstorm of 13 June 1984. *J. Atmos. Oceanic Technol.*, **7,** 104–113.

Balakrishnan, N., and D. S. Zrnić, 1990: Use of polarization to characterize precipitation and discriminate large hail. *J. Atmos. Sci.*, **47,** 1525–1540.

Battan, L. J., 1973: *Radar Observations of the Atmosphere.* University of Chicago Press, 323 pp.

——, and C. F. Bohren, 1986: Attenuation of microwaves by spherical hail. *J. Climate Appl. Meteor.*, **25,** 1155–1159.

Blanchard, D. O., and K. W. Howard, 1986: The Denver hailstorm of 13 June 1984. *Bull. Amer. Meteor. Soc.*, **67,** 1123–1131.

Bluestein, H. B., and G. R. Woodall, 1990: Doppler-radar analysis of a low-precipitation severe storm. *Mon. Wea. Rev.*, **118,** 1640–1664.

Brandes, E. A., 1983: Relationships between thunderstorm mesoscale circulation and tornadogenesis. Ph.D. dissertation, University of Oklahoma, 185 pp.

Bringi, V. N., J. Vivekanandan, and J. D. Tuttle, 1986a: Multiparameter radar measurements in Colorado convective storms. Part I: Graupel melting studies. *J. Atmos. Sci.*, **43,** 2545–2563.

——, ——, and ——, 1986b: Multiparameter radar measurements in Colorado convective storms. Part II: Hail detection studies. *J. Atmos. Sci.*, **43,** 2564–2577.

Browning, K. A., and G. B. Foote, 1976: Airflow and hailgrowth in supercell storms and some implications for hail suppression. *Quart. J. Roy. Meteor. Soc.*, **102,** 449–533.

Caylor, I. C., and A. J. Illingworth, 1987: Radar observations and modeling of warm rain initiation. *Quart. J. Roy. Meteor. Soc.*, **113,** 1171–1191.

Cheng, L., and M. English, 1983: A relationship between hailstone concentration and size. *J. Atmos. Sci.*, **40,** 204–213.

Conway, J. W., and M. L. Weisman, 1988: An investigation into the splitting and propagation of the 13 June 1984 Denver hailstorms. *Proc. 15th Conf. Severe Local Storms,* Baltimore, MD, Amer. Meteor. Soc., 276–279.

Danielsen, E. F., R. Bleck, and D. A. Morris, 1972: Hailgrowth by stochastic collection in a cumulus model. *J. Atmos. Sci.*, **29,** 135–155.

Doswell, C. A., 1980: Synoptic-scale environments associated with High Plains severe thunderstorms. *Bull. Amer. Meteor. Soc.*, **61,** 1388–1399.

Doviak, R. J., and D. S. Zrnić, 1984: *Doppler Radar and Weather Observations.* Academic Press, 458 pp.

Foote, G. B., 1985: Aspects of cumulonimbus classification relevant to the hail problem. *J. Rech. Atmos.*, **19,** 61–74.

Golestani, Y., V. Chandrasekar, and V. N. Bringi, 1989: Intercomparison of multiparameter radar measurements. *Proc. 24th Conf. Radar Meteorology,* Tallahassee, FL, Amer. Meteor. Soc., 309–314.

Herzegh, P. H., and R. E. Carbone, 1984: The influence of antenna illumination function characteristics on differential reflectivity measurements. *Proc. 22d Conf. Radar Meteorology,* Zurich, Amer. Meteor. Soc., 281–286.

——, and A. R. Jameson, 1992: Observing precipitation through dual-polarization radar measurements. *Bull. Amer. Meteor. Soc.*, **73,** 1365–1374.

Heymsfield, A. J., 1982: A comparative study of the rates of development of potential graupel and hail embryos in high plains storms. *J. Atmos. Sci.*, **39,** 2867–2897.

——, A. R. Jameson, and H. W. Frank, 1980: Hailgrowth mechanisms in a Colorado storm. Part II: Hail formation processes. *J. Atmos. Sci.*, **37,** 79–1807.

Illingworth, A. J., J. W. F. Goddard, and S. M. Cherry, 1987: Polarization radar studies of precipitation development in convective storms. *Quart. J. Roy. Meteor. Soc.*, **113,** 469–489.

——, ——, and ——, 1986: Detection of hail by dual-polarization radar. *Nature,* **320,** 431–433.

Knight, N. C., and M. English, 1983: Patterns of hailstone embryo type in Alberta Hailstorms. *J. Rech. Atmos.*, **14,** 325–332.

Leitao, M. J., and P. A. Watson, 1984: Application of dual linearly polarized radar data to prediction of microwave path attenuation at 10–30 GHz. *Radio Sci.*, **19,** 209–221.

Liu, J., and P. H. Herzegh, 1986: Differential reflectivity signatures in ice-phase precipitation: Radar–aircraft comparisons. *Proc. 23d Conf. Radar Meteorology,* Snowmass, CO, Amer. Meteor. Soc., 59–61.

Maddox, R. A., D. M. Rodgers, W. Deitrich, and D. L. Bartels, 1981: Meteorological settings associated with significant convective storms in Colorado. NOAA Tech. Memo. ERL OWRM-4, 73 pp.

Matson, R. J., and A. W. Huggins, 1980: The direct measurement of the sizes, shapes and kinematics of falling hailstones. *J. Atmos. Sci.*, **37,** 1107–1125.

Meischner, P. F., V. N. Bringi, D. Heimann, and H. Holler, 1991: A squall line in Southern Germany: Kinematics and precipitation formation as deduced by advanced polarimetric and Doppler radar measurements. *Mon. Wea. Rev.*, **119,** 678–701.

Miller, L. J., J. D. Tuttle, and C. K. Knight, 1988: Airflow and hailgrowth in a severe northern High Plains supercell. *J. Atmos. Sci.*, **45,** 736–762.

——, ——, and G. B. Foote, 1990: Precipitation production in a large Montana hailstorm: Airflow and particle growth trajectories. *J. Atmos. Sci.*, **47,** 1619–1646.

Nelson, S. P., 1983: The influence of storm flow on hail growth. *J. Atmos. Sci.*, **40,** 1965–1983.

——, and R. A. Brown, 1982: Multiple Doppler radar derived vertical velocities in thunderstorms. NOAA Tech. Memo. ERL NSSL-94, 21 pp.

——, and ——, 1987: Error sources and accuracy of vertical velocities computed from multiple-Doppler radar measurements in deep convective storms. *J. Atmos. Oceanic Technol.*, **4,** 233–238.

——, and N. C. Knight, 1987: The hybrid multicellular-supercellular storm—An efficient hail producer. Part I: An archetypal example. *J. Atmos. Sci.*, **44**, 2042–2059.

Oye, R., and R. E. Carbone, 1981: Interactive Doppler editing software. *Proc. 20th Conf. Radar Meteorology*, Boston, Amer. Meteor. Soc., 683–689.

Pflaum, J. C., 1982: Hail growth studies within a Doppler-radar reconstructed supercell. *Proc. 12th Conf. Severe Local Storms*, San Antonio, TX, Amer. Meteor. Soc., 1–4.

Pruppacher, H. R., and K. V. Beard, 1970: A wind tunnel investigation of the internal circulation and shape of water drops falling at terminal velocity in air. *Quart. J. Roy. Meteor. Soc.*, **96**, 235–257.

Rasmussen, R. M., and A. J. Heymsfield, 1987a: Melting and shedding of graupel and hail. Part I: Model physics. *J. Atmos. Sci.*, **44**, 2754–2763.

——, and ——, 1987b: Melting and shedding of graupel and hail. Part III: Investigation of the role of shed drops as hail embryos in the 1 August CCOPE severe storm. *J. Atmos. Sci.*, **44**, 2783–2803.

Rinehart, R. E., and J. D. Tuttle, 1982: Antenna beam patterns and dual-wavelength processing. *J. Appl. Meteor.*, **21**, 1865–1880.

Seliga, T. A., and V. N. Bringi, 1976: Differential reflectivity measurements at orthogonal polarization for measuring precipitation. *J. Appl. Meteor.*, **15**, 69–76.

Tuttle, J. D., and R. E. Rinehart, 1983: Attenuation correction in dual-wavelength analysis. *J. Climate Appl. Meteor.*, **22**, 1914–1921.

——, V. N. Bringi, H. D. Orville, and F. J. Kopp, 1989: Multiparameter radar study of a microburst: Comparison with model results. *J. Atmos. Sci.*, **46**, 601–620.

Weisman, M. L., and J. B. Klemp, 1984: The structure and classification of numerically simulated convective storms in directionally varying wind shear. *Mon. Wea. Rev.*, **112**, 2479–2498.

Ziegler, C. L., P. S. Ray, and N. C. Knight, 1983: Hail growth in an Oklahoma multicell storm. *J. Atmos. Sci.*, **40**, 1768–1791.

Zrnić, D. S., 1987: Three-body scattering produces precipitation signature of special diagnostic value. *Radio Sci.*, **22**, 76–86.